ELEMENTA
Science of the Anthropocene

Silber, I and Shupe, MD. 2022. Insights on sources and formation mechanisms of liquid-bearing clouds over MOSAiC examined from a Lagrangian framework. *Elem Sci Anth*, 10: 1. DOI: https://doi.org/10.1525/elementa.2021.000071

RESEARCH ARTICLE

Insights on sources and formation mechanisms of liquid-bearing clouds over MOSAiC examined from a Lagrangian framework

Israel Silber[1,*] and Matthew D. Shupe[2,3]

Understanding Arctic stratiform liquid-bearing cloud life cycles and properly representing these life cycles in models is crucial for evaluations of cloud feedbacks as well as the faithfulness of climate projections for this rapidly warming region. Examination of cloud life cycles typically requires analyses of cloud evolution and origins on short time scales, on the order of hours to several days. Measurements from the recent Multidisciplinary drifting Observatory for the Study of Arctic Climate (MOSAiC) expedition provide a unique view of the current state of the central Arctic over an annual cycle. Here, we use the MOSAiC radiosonde measurements to detect liquid-bearing cloud layers over full atmospheric columns and to examine the cloud-generating air masses' properties. We perform 5-day (120 h) back-trajectory calculations for every detected cloud and cluster them using a unique set of variables extracted from these trajectories informed by ERA5 reanalysis data. This clustering method enables us to separate between the air mass source regions such as ice-covered Arctic and midlatitude open water. We find that moisture intrusions into the central Arctic typically result in multilayer liquid-bearing cloud structures and that more than half of multilayer profiles include overlying liquid-bearing clouds originating in different types of air masses. Finally, we conclude that Arctic cloud formation via prolonged radiative cooling of elevated stable subsaturated air masses circulating over the Arctic can occur frequently (up to 20% of detected clouds in the sounding data set) and may lead to a significant impact of ensuing clouds on the surface energy budget, including net surface warming in some cases.

Keywords: Arctic clouds, Supercooled clouds, Cloud formation mechanisms, MOSAiC, ERA5, Lagrangian analysis

1. Introduction

Characterization of Arctic stratiform liquid-bearing cloud life cycles is an essential component of understanding ocean–cryosphere–atmosphere feedbacks and present and projected regional and global climate patterns (e.g., Bennartz et al., 2013; Kay et al., 2016; Lenaerts et al., 2017; Tan & Storelvmo, 2019). While the radiative forcing of Arctic clouds has been linked to the ensuing extent of Arctic sea ice in the following season or year (e.g., Kay et al., 2008; Persson, 2012; Cox et al., 2016), examination of cloud life cycles often requires the analysis of shorter term patterns. At these short time scales, on the order of hours to several days, polar liquid-bearing cloud (henceforth referred to as cloud) fields frequently impose intense instantaneous surface radiative forcing (e.g., Intrieri et al., 2002; Shupe and Intrieri, 2004; Dong et al., 2010; Miller et al., 2015; Turner et al., 2018; Silber et al., 2019a) and have been shown to impact ice sheet melt (e.g., Bennartz et al., 2013; Nicolas et al., 2017) and melt-water runoff (e.g., Van Tricht et al., 2016). On the other hand, Arctic cloud occurrence and characteristics also demonstrate susceptibility to low-level and surface conditions (e.g., static stability and sea ice cover), which can limit moisture availability (e.g., relative to open water), influence the exchange of heat with the atmosphere, and modulate atmospheric stability (e.g., Herman and Goody, 1976; Curry et al., 1996; Schweiger et al., 2008; Kay and Gettelman, 2009; Kay et al., 2011).

The formation of these clouds can occur as a result of moisture mass fluxes into the region originating in warming-induced expanding open-water Arctic sectors (e.g., Boisvert et al., 2015) or lower latitudes (e.g., Doyle et al., 2011; Tjernström et al., 2015; Rinke et al., 2019), and/or persistent radiative cooling of subsaturated stable air (e.g., Curry et al., 1996; Garrett et al., 2009; Simpfendoerfer et al., 2019). Moisture mass fluxes into the Arctic are dominated by dynamic intrusion events characterized by meridional transport of warm and moist air (e.g.,

[1] Department of Meteorology and Atmospheric Science, Pennsylvania State University, University Park, PA, USA

[2] Cooperative Institute for Research in Environmental Science, Boulder, CO, USA

[3] NOAA/Physical Sciences Laboratory, Boulder, CO, USA

* Corresponding author:
Email: ixs34@psu.edu

Herman and Goody, 1976; Pithan et al., 2018), which are frequently driven by cyclones (e.g., Woods et al., 2013; Fearon et al., 2021) and can occur year-round (e.g., Pithan et al., 2014; You et al., 2021). These intrusion events are frequently associated with the formation and development of low-level clouds able to modulate the thermodynamic atmospheric profile, a process known as Arctic air formation (e.g., Curry, 1983; Pithan et al., 2014). During Arctic air formation, clouds often become optically thick and can induce strong radiative forcing on (often ice-covered) Arctic surfaces (e.g., Tjernström et al., 2019).

Arctic stratiform cloud formation and persistence is not limited to warm air advection, which occurs roughly 10% of the time (Liu and Barnes, 2015). The typical residence time of moisture over the Arctic ranges between 5 and 8 days, based on different estimates (e.g., Läderach and Sodemann, 2016; Woods and Caballero, 2016; van der Ent and Tuinenburg, 2017), suggesting that Arctic air may also circulate over the region for extended periods. This circulation provides sufficient time for clouds to form near the surface or at elevated levels via radiative cooling, ultimately driving droplet condensation (e.g., Garrett et al., 2009; Simpfendoerfer et al., 2019) and the associated cloud feedbacks.

To date, Arctic cloud occurrence and characteristics have not been quantitatively linked with cloud formation mechanisms such as warm moist air intrusion events, other diffused moisture intrusions with small magnitudes, or circulating Arctic air with prolonged radiative cooling. Such a case-by-case approach can benefit case studies and enable the evaluation of the frequency-wise significance of different cloud forming mechanisms and sources.

Here, we examine the characteristics of some of these different cloud formation mechanisms by combining Eulerian observations of the central Arctic atmosphere collected over sea ice during the recent Multidisciplinary drifting Observatory for the Study of Arctic Climate (MOSAiC) expedition (Shupe et al., 2020; Shupe et al., 2021) with Lagrangian back-trajectory model calculations. We estimate the source latitudes of warm moist air intrusion events and evaluate the relative occurrence of clouds forming from prolonged radiative cooling of air circulating over the Arctic or originating in mid- to high-latitude continental air.

2. Methodology

2.1. Cloud detection

To detect clouds over the full atmospheric column, we use the 6-hourly sounding measurements performed during the MOSAiC field campaign from onboard the *Polarstern* vessel between October 4, 2019, and September 19, 2020 (a total of 1,362 sounding profiles; Maturilli et al., 2021). We exclude from the analysis periods in which the *Polarstern* was transiting very close to the sea-ice edge or over open water based on the expedition log: September 20 to October 3, 2019, June 2 to June 10, 2020, July 31 to August 13, 2020, and September 20 to October 1, 2020. The sounding measurement profiles are interpolated onto a 15 m vertical grid, after which cloudy grid cells are determined using a relative humidity (RH) threshold of 96%, which considers the 4 percentage points measurement uncertainty of the Vaisala RS-41 radiosondes (Holdridge, 2020) used during MOSAiC. This RH threshold method was robustly validated against high spectral resolution lidar (HSRL; Eloranta, 2005) measurements in previous Arctic studies (see Silber et al., 2020; Figure S1) and also showed good correspondence with the HSRL liquid cloud base height data product produced for MOSAiC (Silber et al., 2018; Bambha et al., 2019; Silber et al., 2021b; see Figure S1 in the Supplemental Material). After cloudy grid cells are detected, vertically adjoining cloud layers are concatenated if vertically distant by less than 30 m (approximately 7 raw sounding samples), followed by the removal of detected layers shallower than 30 m. This small depth threshold enables the inclusion of commonly occurring very shallow Arctic layers in the analysis, while still excluding potential false detections in moist atmospheric layers, in which the air is only slightly subsaturated.

By applying this simple RH-based cloud detection methodology, we find that 997 profiles in the sounding data set contain cloud layers. That is a liquid-bearing cloud occurrence of 73%, approximately 17 percentage points higher than the occurrence reported over the Arctic sea ice approximately 2 decades ago based on measurements from the Surface Heat Budget of the Arctic Ocean (SHEBA; Uttal et al., 2002) field campaign (see Shupe, 2011). This different cloud occurrence during MOSAiC relative to SHEBA could originate in various sources such as the long-term sea-ice decline or the position of the MOSAiC deployment onboard the *Polarstern* vessel relative to the sea-ice edge or in the Atlantic–Arctic Sector, which requires an in-depth analysis beyond the scope of this study.

A total of 2,107 cloud layers (93% supercooled) are detected in the sounding data set, half of which (49%) being of a single cloud layer per sounding profile (see **Figure 1a**). Multiple cloud layers are detected in 51% of the cloud-bearing sounding profiles, a similar occurrence rate to the SHEBA observations (Shupe et al., 2006), with 2 detected cloud layers occurring in more than 1 of every 5 cloud-bearing profiles, and profiles with 4 or more overlying cloud layers occurring in approximately 16% of cases (**Figure 1a**).

2.2. Back trajectories

With the information about cloud occurrence over MOSAiC, we run 5-day (120-h) back-trajectory calculations using the Hybrid Single-Particle Lagrangian Integrated Trajectory model (Stein et al., 2015) informed by reanalysis data from ERA5 (Hersbach et al., 2020). When compared with Arctic surface (2-m), near-surface (10-m), and sounding measurements, ERA5-resolved wind fields essential for these back-trajectory calculations showed high correlation coefficients greater than 0.9 and biases smaller than 10%, up to 0.6 m/s near the surface and 0.3 m/s at higher levels (e.g., Graham et al., 2019a; Graham et al., 2019b; Renfrew et al., 2021). While these studies indicated that ERA5 tends to produce relatively larger surface and near-surface errors, they also found that it generally outperforms other reanalysis data sets in the prediction of wind, temperature, and moisture fields, all of which are used in

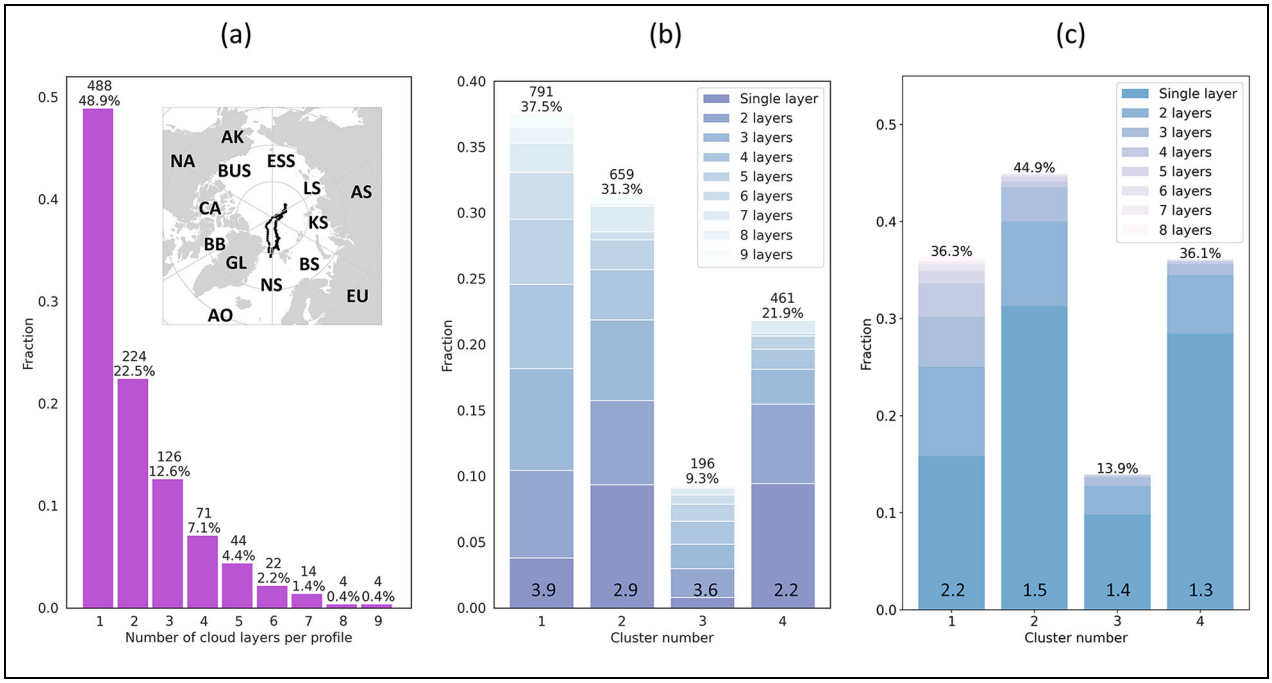

Figure 1. (a) Histogram of the number of liquid-bearing cloud layers detected per sounding profile in the MOSAiC sounding data set. The number and percentage above each bar designate the total number of profiles and the percentage relative to all liquid-bearing cloud profiles, respectively. The inset map shows the MOSAiC sounding release coordinates (black dots) together with the locations of (from top left to bottom right) North America (NA), Canadian Archipelago (CA), Baffin Bay (BB), Atlantic Ocean (AO), Alaska (AK), Beaufort Sea (BUS), Greenland (GL), Norwegian Sea (NS), East Siberian Sea (ESS), Laptev Sea (LS), Kara Sea (KS), Barents Sea (BS), Asia (AS), and Europe (EU). (b) Histogram of the 4 air mass back-trajectory clusters. The color scale represents the distribution of the total number of cloud layers detected in sounding profiles containing one or more of the clustered air mass (corresponding to a detected cloud layer), with the mean number of layers given at the base of each bar. The number and percentage above each bar denote the total number of air masses associated with every cluster and their percentage relative to all examined air masses (equal to the total number of cloud layers detected in the sounding data set). (c) Similar to the middle panel, but with the color scale designating the distribution of the number of cloud layers in the sounding profile associated with the depicted clusters (mean values shown at the base of each bar). Fraction of cloud-bearing profiles with detected clouds associated with the depicted clusters are represented in the y-axis and corresponding percentages are given above each bar (note that because a multilayer sounding profile may exhibit clouds attributed with different clusters, the sum of the fractions is greater than 1). DOI: https://doi.org/10.1525/elementa.2021.000071.f1

this trajectory analysis. This apparent superiority of ERA5 was indicated even when compared with nonassimilated observational data (see Graham et al., 2019b).

Considering the typical residence time of moisture in the atmosphere, the calculated 5-day trajectories likely cover the vast majority of air mass moisture sources resulting in the observed clouds. The back-trajectories are initialized at the middle of each detected cloud layer. Full 5-day trajectories confined to the polar latitudes (>60°N) are calculated using the full resolution of the ERA5 data product (0.25°), while trajectories extending south of 60°N are fully calculated using the 1.00° data product.

2.3. Back-trajectory data set clustering

Once the MOSAiC cloudy air mass back-trajectory data set is produced, we perform unsupervised clustering of the resultant trajectories, which enables us to gain insights into potential cloud sources. The limited number of trajectories (samples) requires a restricted number of classification input parameters to allow consistent convergence on a set number of clusters. Because the formation and evolution of polar stratiform clouds depend on air mass moisture hysteresis and the potential dynamic and thermodynamic surface influence (e.g., the impact of sea-ice cover vs. open water), we choose to use 4 variables calculated using ERA5 data fields (sea-ice cover, specific humidity, etc.) along air mass back-trajectories as the basis for the cluster classification:

- Time (in hours) since the last passage over open water, Δt_{lo}. Open water grid cells are defined here as sea-surface grid cells with sea-ice cover fraction smaller than 0.15. The sea-ice cover fraction data are determined by ERA5 based on the Operational Sea Surface Temperature and Sea Ice Analysis (Donlon et al., 2012). The utilized threshold of 0.15 is consistent with the definition by the National Snow and Ice Data Center

(https://nsidc.org/) of "not ice-covered" over 25 × 25 km discretized grid cells. Note that the maximum value of Δt_{lo} is 120 h (5 days).

- The mean sea-ice cover along the trajectory since the last passage over open water (i.e., during Δt_{lo}), $\overline{\mathrm{SIC}}$. Note that under this definition, during Δt_{lo} the passage of air masses over continents, which could serve as a significant source of Arctic moisture during summer (e.g., Vázquez et al., 2016; Naakka et al., 2019) reduces $\overline{\mathrm{SIC}}$.
- The normalized difference between the air mass–specific humidity (q_v) over MOSAiC (t_{mos}) and the last passage over water (t_{lo}), $\widetilde{\Delta q_v}$, calculated as:
- $\widetilde{\Delta q_v} = \frac{q_v(t_{\mathrm{mos}}) - q_v(t_{lo})}{q_v(t_{\mathrm{mos}})}$.
- The normalization mitigates the otherwise strong seasonal signal of the q_v variable. We note that some seasonal influence still exists in our clustering, mainly owing to the dependence on $\overline{\mathrm{SIC}}$ and Δt_{lo}.
- The mean ratio of the air mass height (z) to the planetary boundary layer height (PBLH) along the trajectory since t_{lo}, $\overline{z/\mathrm{PBLH}}$. The PBLH diagnostic used here is taken from the ERA5 output (ECMWF, 2016, Ch. 3.10) and is based on a bulk Richardson number algorithm proposed by Vogelezang and Holtslag (1996), which was validated by Seidel et al. (2012). $\overline{z/\mathrm{PBLH}}$ values smaller than 1 indicate significant coupling with the surface along the air mass trajectory. Values larger, but not significantly larger, than 1 could still suggest some interaction with the surface during at least part of the air mass advection over land, open water, or sea ice, as also suggested by the conceptual model of Arctic air formation (e.g., Pithan et al., 2018). For example, the first and third quartiles of $\overline{z/\mathrm{PBLH}}$ in cases where air masses have $z/\mathrm{PBLH} < 1$ for at least 1 h are 1.1 and 5.7.

These 4 variables show little correlation with each other and hence likely enable better coverage of the trajectory parameter space (see contour and scatterplot panels in **Figure 2**). For this reason, we omitted the use of temperature-dependent thermodynamic variables such as the virtual potential temperature (θ_v), which presents a high correlation with q_v over the Arctic (e.g., Nygård et al., 2020; see also **Figure 3a2** and **b1**). We note that while ERA5 seemingly outperforms other reanalysis data sets in its bulk cloud representation over the Arctic (e.g., Yao et al., 2020; Gu et al., 2021), there has been evidence that it often shows large errors in representing Antarctic supercooled cloud occurrence and characteristics in a case-by-case evaluation, indicating potential-related model weaknesses (Silber et al., 2019b). Because an additional evaluation of Arctic supercooled cloud representation in ERA5 is required, we omit condensate diagnostics such as cloud occurrence, inception time, and condensed water amount from this back-trajectory analysis.

The 6 h separating consecutive sounding profiles mean that trajectories from consecutive times are loosely dependent in most cases, given that from an Eulerian perspective, most Arctic clouds persist for periods shorter than 6 h (e.g., Shupe, 2011; Shupe et al., 2011). This assumption is further supported by a separate analysis of cloud continuation in consecutive sounding profiles, performed by allowing cloud base height to change at a mean rate magnitude smaller than 0.5 cm/s, which indicated that about 4 out of 5 detected clouds do not persist in more than a single sounding profile (not shown).

To perform the classification, we use a Bayesian Gaussian mixture model algorithm with a Dirichlet process prior (Attias, 2000; Blei and Jordan, 2006; Pedregosa et al., 2011), which among other advantages enables uneven resultant cluster sizes. To determine the suitable number of clusters to use, we run the classification algorithm using 3–10 clusters and search for the best and most consistent separation between clusters determined by the Silhouette Coefficient (Rousseeuw, 1987) calculated for 1,000 iterations of the classification algorithm (a total of 8,000 runs). The classification results using 4 clusters provide the most robust results with a mean Silhouette Coefficient of 0.25 ± 0.01, suggesting that some overlap still exists between the different clusters. However, confusion (similarity) matrices calculated for pairs of the first run with the other iterations (all using 4 clusters) indicate a small uncertainty of 1%, defined here as the mean percentage of false positive or negative cases when treating the first run as the ground truth. Thus, using 4 clusters, we receive the best cluster separation (given the input variables we use) and a high consistency of the classification results.

3. Results

Figure 1 depicts the occurrence fraction of the 4 resulting clusters together with the distribution of the total number of cloud layers per profile containing one or more clustered air masses (Panel b) and the distribution of the number of cloud layers per profile attributed to the same cluster (Panel c). For example, a profile with a total of 4 detected cloud layers, 3 of which are associated with Cluster 1 and 1 of which is associated with Cluster 2, would translate in Panel b to 3 cluster 1 samples equal to 4 and another Cluster 2 sample equals to 4, while for Panel c, this profile would be counted as a Cluster 1 sample equals to 3 and another Cluster 2 sample equals to 1. **Figure 4** illustrates the air mass back-trajectory paths associated with each cluster, while **Figure 5** shows density plots of each cluster over the 5-day trajectory path, the first 12 h of the trajectory (close to the MOSAiC deployment site onboard the *Polarstern*), and the last 24 h of the trajectories (potential source region). The general attributes of the 4 clusters are given in **Table 1**, while the likelihood of an air mass associated with a given cluster to be followed by an air mass associated with 1 of the 4 clusters in the consecutive sounding profile (after approximately 6 h) is shown in **Table 2**.

Air masses associated with these 4 clusters can be principally described by the following features:

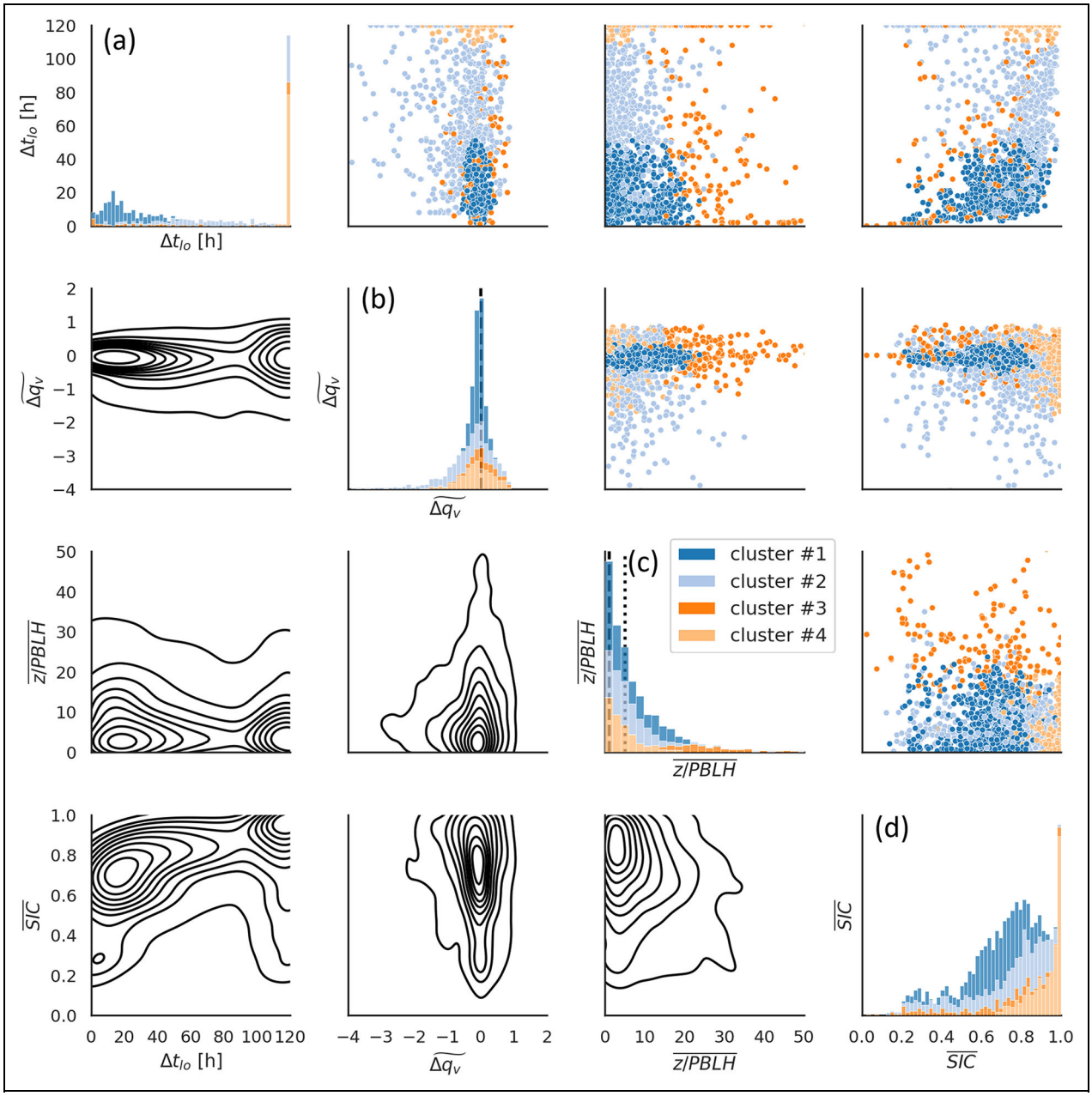

Figure 2. Cloudy air mass back-trajectory statistics: (from top to bottom or left to right) the period since the last passage over open water (Δt_{lo}), the normalized difference between the air mass specific humidity (q_v) over MOSAiC and the last passage over open water ($\widetilde{\Delta q_v}$), the mean ratio of air mass height (z) to the planetary boundary layer height (PBLH) since the last passage over open water ($\overline{z/PBLH}$), and the mean sea-ice cover since the last passage over open water, $\overline{SIC}$ (counting overpassed continental regions as sea-ice-free in averaging; see Section 2.3 for details). The different panels depict qualitative 2-dimensional contoured histograms (panels below the diagonal panels), qualitative single variable histograms (diagonal panels) and 2-dimensional scatter plots (panels above the diagonal panels). The bar and marker colors designate the 4 air mass back-trajectory clusters (see legend). The dashed vertical line in Panel b denotes a $\widetilde{\Delta q_v}$ value of 0 (no change in specific humidity), while the dashed and dotted vertical lines in Panel c designate $\overline{z/PBLH}$ values of 1 (full surface coupling) and 5 (likely some interaction with the surface below this value; see text), respectively. DOI: https://doi.org/10.1525/elementa.2021.000071.f2

- Clusters 1: moist air intrusions mainly from open water at low- to high-latitudes onto patchy sea-ice-covered regions.
- Clusters 2: moist air intrusions mainly from open water at mid- to high-latitudes onto patchy or fully covered sea-ice regions.
- Cluster 3: elevated decoupled air masses mostly of coastal or continental origin.
- Cluster 4: Arctic air circulating over sea ice.

These air masses are most likely to be followed by air masses associated with the same cluster (diagonal values

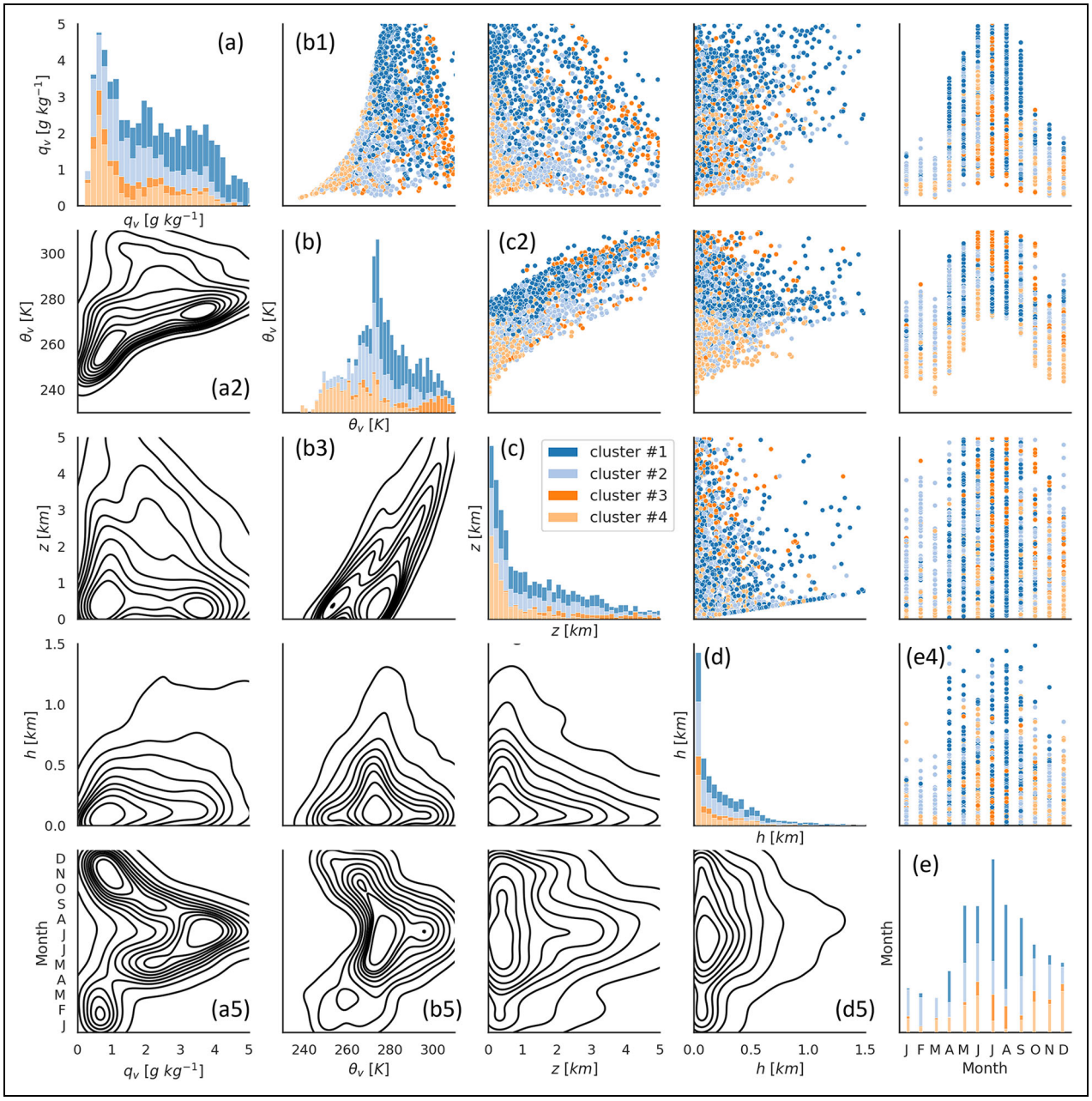

Figure 3. As in Figure 2 but with the different histograms and scatter plots generated for q_v, virtual potential temperature (θ_v), height (z), geometrical thickness (h), and the corresponding month of liquid-bearing cloud layers observed over MOSAiC. DOI: https://doi.org/10.1525/elementa.2021.000071.f3

in **Table 2**). This result emphasizes the tendency of synoptic-scale weather patterns to influence the examined Arctic region for a few days (e.g., Serreze and Barry, 1988; Simmonds et al., 2008; Papritz and Dunn-Sigouin, 2020), longer than the 6 h separating consecutive sounding profiles. The likelihoods of one or more Cluster 4 air masses to be observers following or prior to one or more Cluster 1 air masses are 0.02 and 0.07, respectively, which manifest the fundamental contrasts between these 2 clusters. On the other hand, Cluster 3 air masses are nearly as likely as Cluster 1 air masses to overpass the MOSAiC deployment site following cluster 1 air masses (first row in **Table 2**) and also tend to occur following Cluster 2 air masses in more than 1 of 4 cases (second row in **Table 2**). This tendency of Cluster 3 air masses to follow air masses associated with Clusters 1 and 2 is presumably influenced by the overlap with some of these two clusters' air masses potential continental origin over northern Asia and Europe.

However, these 2 clusters, each accounting for roughly one third of all cloud layers detected in the MOSAiC sounding data set (69% together relative to all cloud layers; see **Figure 1b**), primarily represent cases of moisture advection onto the Arctic sea ice from various marine sources: from the Atlantic Ocean at low- to midlatitudes and the Norwegian to the East Siberian Sea in the case of cluster 1 (see **Figure 1a**'s inset for orientation), and the eastern Arctic from the Norwegian to the Laptev Sea with

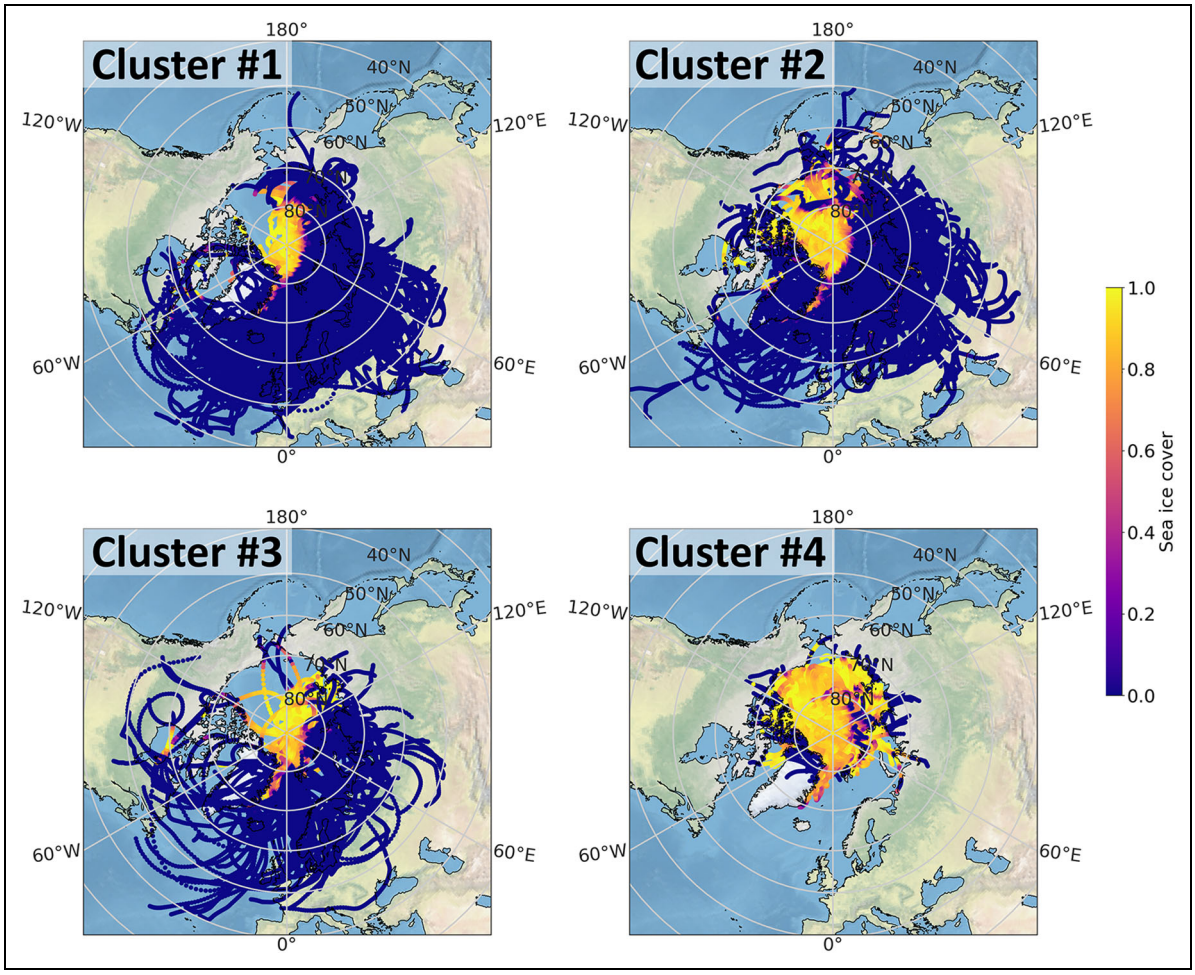

Figure 4. Back trajectories associated with each of the 4 clusters. The color scale of the depicted paths represents the sea-ice cover fraction. DOI: https://doi.org/10.1525/elementa.2021.000071.f4

a number of cases originating in the Beaufort Sea and the Canadian Archipelago in the case of Cluster 2 (**Figures 4** and **5**). Thus, the vast majority of the clouds in Cluster 1 and most of the cases in Cluster 2 are likely the results of poleward warm moist intrusions.

These poleward warm moist intrusions associated with Clusters 1 and 2 are typified by multilayer cloud profiles as well as geometrically thicker clouds over MOSAiC (**Figures 1b** and **3d**), with a maximum average of approximately 3.9 layers per profile and an average cloud thickness of approximately 420 m in the case of Cluster 1. Cluster 3 air masses also occur in profiles containing a similar number of cloud layers on average (3.6), but those air masses do not tend to produce multiple cloud layers simultaneously (**Figure 1c**).

The frequently occurring large number of overlying cloud layers that also tend to be thicker in Cluster 1 is likely affected by its associated cases occurring preferentially during the summer months (**Figure 3d5** and **e**). The larger sectors of the troposphere with relatively greater temperatures (within the heterogeneous freezing regime) combined with large amounts of moisture (**Figure 3b1**) during summer months (**Figure 3a5**, **b3**, and **b5**) facilitate the formation of clouds over MOSAiC at a wide range of altitudes in cluster 1 (**Figure 3c**, **c2**, and **e4**). This cluster is characterized by periods of air mass advection over sea ice prior to the MOSAiC overpass (Δt_{lo}) mostly shorter than a day (**Figure 2a**). Most of the sea ice overpassed by these Cluster 1 air masses is composed of rather patchy and occasionally probably melting, ice floes (**Figure 2d**) and located at relatively lower latitudes (see **Figure 5**, middle), thereby enabling a supplemental surface-based moisture source (open water areas). Such an augmenting surface moisture source is most likely relevant when $\overline{z/\mathrm{PBLH}}$ is small, hence indicating some interaction with the surface over the course of the air mass trajectory over sea ice. These cases with potential interaction with the surface account for approximately half of Cluster 1's air masses when an arbitrarily selected upper $\overline{z/\mathrm{PBLH}}$ threshold value of 5 is used (dotted line in **Figure 2c**). This large threshold value also considers that ERA5's PBLH diagnostic is influenced by the relatively large errors in the representation of near-surface temperatures and temperature inversions over polar regions (e.g., Graham et al., 2019b; Silber et al., 2019b) and could exhibit uncertainties greater than 50%, especially in the first several hundred meters above ground level (see Seidel et al., 2012, their figure 2).

Even though Cluster 1 is characterized by the greatest amounts of moisture relative to all other clusters

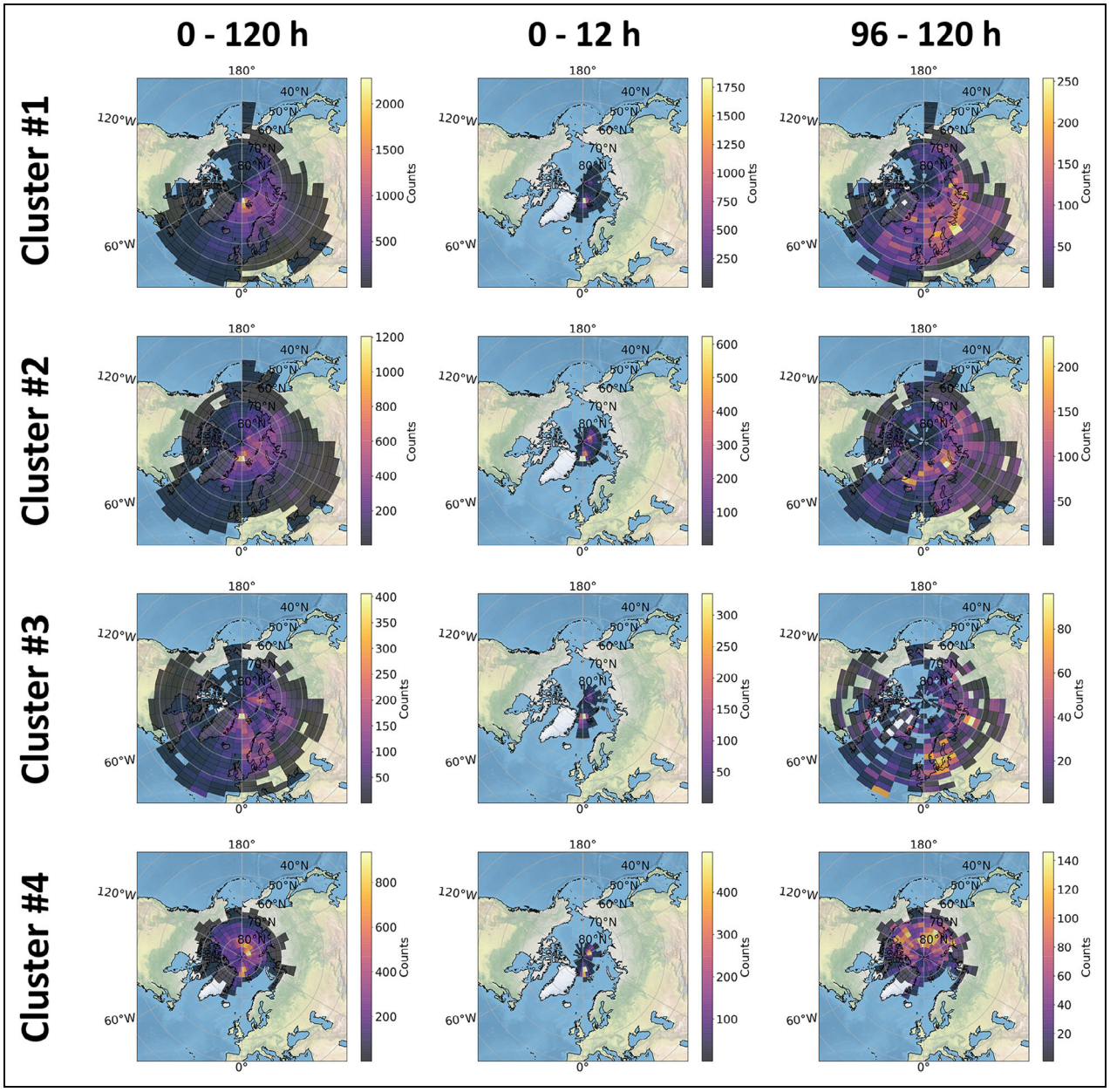

Figure 5. Density maps of air mass coordinates in every cluster (rows) at different temporal ranges of the back-trajectory paths (columns). These temporal ranges represent the full trajectory paths (0–120 h; left), periods close both spatially and temporally to the MOSAiC observations (0–12 h; middle), and plausible air mass sources (96–120 h; right). The color scale represents counts in each 2.5° latitude × 10.0° longitude grid cell. DOI: https://doi.org/10.1525/elementa.2021.000071.f5

(**Figure 3a**), the clouds formed from the associated air masses can deposit, via precipitation and/or mixing, only a limited relative amount of moisture over the sea ice before the MOSAiC overpass, indicated by the small and negative $\widetilde{\Delta q_v}$ (**Figure 2b**). This comparatively small loss of moisture is presumably the result of the short Δt_{lo} (**Figure 2a**). Δt_{lo} is much longer in Cluster 2, allowing an extended passage of relatively warm and moist air over colder sea ice and overlying atmosphere, thereby inducing cloud formation. Precipitation formation and sedimentation and/or cloud-induced vertical mixing with dryer air resulting in the removal of moisture from this cluster's air masses can consequently lead to significant moisture removal, suggested by negative $\widetilde{\Delta q_v}$ values with the largest magnitudes in Cluster 2 relative to the other 3 clusters. We note that some of these large $\widetilde{\Delta q_v}$ magnitudes might be the result of reanalysis model microphysics that are too aggressive, resulting in excess production of ice (cf. Silber et al., 2019b); this topic might benefit from a dedicated study.

Clusters 3 and 4 also show a large number of cases with negative $\widetilde{\Delta q_v}$ but with smaller magnitudes than in the warm moist air advection Cluster 2. With a consistent decoupled state (Cluster 3; **Figure 2c**) or at least 5 days without an open water overpass (Cluster 4; **Figure 2a**), the air masses associated with these 2 clusters are

Table 1. Air mass back-trajectory cluster general attributes. DOI: https://doi.org/10.1525/elementa.2021.000071.t1

Cluster Number	Typical Source (Figures 4 and 5)	Typical Level and Coupling (Figures 3c and 2c)	Typical Time Since Open Water Overpass and $\overline{\text{SIC}}$ (Figure 2a and d)	Season (Figure 3d)
1	Low- to high-latitudes, mostly marine	Low- to high-level, frequent coupling	<2.0 days with $\overline{\text{SIC}} < 0.9$	Year-round; most frequent in April–September
2	Mid- to high-latitudes, mostly marine	Low- to high-level, frequent coupling	>0.5 days with variable $\overline{\text{SIC}}$	Year-round
3	Mid- to high-latitudes, mostly coastal Arctic or continental	Mid- to high-level, decoupled	Variable periods with variable $\overline{\text{SIC}}$	Year-round; most frequent in June–August
4	Ice-covered Arctic and coastal Arctic	Low- to mid-level, frequent coupling	$\geq$5.0 days with $\overline{\text{SIC}} > 0.7$	Year-round; most frequent in October–January

$\overline{\text{SIC}}$ denotes mean sea-ice cover since last open water overpass (while counting overpassed continental regions as lack of sea ice in averaging; see Section 2.3). Relevant figures are provided in the title of each column.

Table 2. The likelihood of an air mass associated with 1 of the 4 clusters in a given sounding profile (rows) to be followed by an air mass associated with one of the clusters in the consecutive sounding profile (after approximately 6 h; columns). DOI: https://doi.org/10.1525/elementa.2021.000071.t2

		Proceeding Cluster			
		1	2	3	4
Preceding cluster	1	0.50	0.12	0.36	0.02
	2	0.17	0.41	0.27	0.15
	3	0.18	0.12	0.63	0.07
	4	0.07	0.23	0.19	0.51

All optional pairs are counted separately in multilayer preceding and/or proceeding profiles, resulting in a total of 7,861 samples. For example, if the preceding and proceeding sounding profiles contain 2 and 3 detected layers, respectively, 6 samples would be added to the calculation. The likelihoods are weighted by the inverse of the relative occurrence of each proceeding cluster and normalized such that each row sums up to 1.

generally the driest of all clusters (**Figure 3a**), with Cluster 4's air masses also being the least potentially energetic (**Figure 3b**). The clouds observed over MOSAiC associated with these 2 clusters tend to be shallower (**Figure 3d**), with an average layer thickness of approximately 200 m in each cluster.

Cluster 4 air masses circulate for a prolonged period over central Arctic regions characterized by widespread sea ice (**Figures 4** and **5**) with very high cover (**Figure 2d**), which impedes moisture supply, and hence, generally results in a large potential for moisture loss (e.g., via precipitation) but little potential for moisture gain. Yet, the frequent low-level cloud occurrence associated with this cluster (**Figure 3c**), the $\overline{z/\text{PBLH}}$ values smaller than 5 in approximately two thirds of the cluster cases (**Figure 2c**), and the positive $\widetilde{\Delta q_v}$ values in roughly one third of the cluster's trajectories (**Figure 2b**) suggest that some interaction with the surface does exist occasionally, surmised to be related to relatively lesser $\overline{\text{SIC}}$. This hypothesis is supported by a separate back-trajectory analysis using 1-h intervals (not shown) in which we found using the 2-sample Kolmogorov–Smirnov test (Hodges, 1958) a statistically significant smaller sea ice cover, by 1% on average, in time steps with positive relative to negative Δq_v for Cluster 4 cases with $z/\text{PBLH} < 5$ (note the nonaveraged variables), as well as an increasing fraction of positive $\widetilde{\Delta q_v}$ with decreasing $\overline{z/\text{PBLH}}$.

As for the results of Cluster 4, positive $\widetilde{\Delta q_v}$ values occur in approximately one third, approximately one fourth, and half of the air masses associated with Clusters 1, 2, and 3, respectively (**Figure 2b**). Similar to some of Cluster 1 and 2's air masses, Cluster 3's air masses mostly originate in coastal Arctic regions, from the Barents to the Laptev Sea, or continental regions over eastern Greenland, northern Europe, the Canadian Archipelago, and northern Asia (**Figures 4** and **5**). The latter 2 continental sources are known as major moisture sources, mainly during summer (e.g., Jakobson and Vihma, 2010; Gimeno et al., 2019), during which these air masses commonly occur (**Figure 3e** and **e4**), and could therefore contribute to the relatively high frequency of positive $\widetilde{\Delta q_v}$ values (**Figure 2b**). We note that the predominant decoupled state of Cluster 3's air masses (**Figure 2c**) does suggest that the moisture gain mostly results from mixing with other elevated moister air masses or the evaporation and/or sublimation of precipitation from above. The possibility of mixing with moister air masses is supported by Cluster 3 air masses being more likely to emerge over MOSAiC several hours following a warm moist intrusion event associated with Clusters 1 or 2 (third column in **Table 2**), in addition to cases of these 2 clusters with a potential moist continental origin. Contribution of sublimation of precipitation from above to the positive $\widetilde{\Delta q_v}$ is supported by the air masses' RH with

respect to ice (RH_i). The mean RH_i along each trajectory during sea-ice overpass (not shown) exhibits an average value of $78\% \pm 16\%$ in those positive $\widetilde{\Delta q_v}$ Cluster 3 cases (uncertainty represented by the standard deviation) and thereby supports precipitation sublimation as a potential source of the resulting positive $\widetilde{\Delta q_v}$. For comparison, negative $\widetilde{\Delta q_v}$ cases show an average RH_i value of $99\% \pm 10\%$. We note that this potential precipitation sublimation effect is not as significant in the case of Cluster 4, in which the average RH_i in positive $\widetilde{\Delta q_v}$ cases is $88\% \pm 16\%$. Further delineation of the potential sources of positive $\widetilde{\Delta q_v}$ cases requires an Eulerian analysis using additional spatial ERA5 data sets and is beyond the scope of this study.

4. Discussion

Here, we presented a back-trajectory analysis of cloudy air masses detected over MOSAiC, together with classification of the trajectory calculation results into several categories. Robust and consistent clustering procedures of different parameters such as the output variables of these back-trajectory calculations typically require the number of samples to be greater than the number of clustered parameters by two or more orders of magnitude. With about 2,100 samples (number of detected cloud layers in the sounding data set), this criterion provides a major challenge given that every 120-h back-trajectory sample includes 120 variables (for every calculated hour) per air mass parameter (e.g., latitude, longitude, temperature). Even with 24-h trajectory sampling steps, this criterion for the number of variables being 2 orders of magnitude smaller than the number of samples cannot be met. In our analyses, we examined up to 8 different clustered variables (not shown) but essentially found that the clustering methodology did not provide consistent results (relative distribution of cluster occurrence, some cluster properties, etc.) over a set of iterations. However, with the limited number of 4 variables used here (Δt_{lo}, $\overline{SIC}$, $\widetilde{\Delta q_v}$, and $\overline{z/PBLH}$) we were able to produce robust and consistent clustering results. Moreover, the 4 resultant clusters exhibit fairly distinct characteristics, separating circulating Arctic air from continental sources as well as warm moist intrusions onto the sea ice. Thus, we postulate that these variables are useful for Lagrangian analyses of Arctic air masses with reduced seasonal dependence, such as in the analysis conducted here.

The multilayer cloud structures prevalent in Clusters 1 and 2 (**Figure 1b** and **c**) could be related to cyclones propagating into the region providing moisture with potentially variable spatial patterns over great atmospheric depths (e.g., Woods et al., 2013; Binder et al., 2017; Fearon et al., 2021). In addition, this high number of multilayer cases could be related to open water patches and leads associated with diminished sea ice cover (**Figure 2d**), which might consequently result in the vertical distribution of enhanced-moisture layers. However, large uncertainties still exist concerning the impact of such open water patches and ice leads on the formation (e.g., Zulauf and Krueger, 2003; Kay and Gettelman, 2009) or dissipation of clouds (e.g., Li et al., 2020). Some of these ice leads and open water patches can be transient and smaller than the resolution of the satellite data assimilated in ERA5 (Donlon et al., 2012; Hirahara et al., 2016; see also Pinto et al., 2003), thereby contributing to uncertainties in atmospheric near-surface moist processes represented by the reanalysis. By the same token, scarcity of such open water effects could explain the relatively small numbers of overlying cloud layers and multilayer cases in general in the high sea-ice cover Cluster 4 (**Figure 1b** and **c**). However, the complexity of multilayer cloud dynamical and radiative interactions, especially in the case of the commonly occurring Arctic mixed-phase clouds (e.g., Verlinde et al., 2013; Chen et al., 2020), further complicates the examination of these potential sources, and hence, likely requires case-by-case analyses that are beyond the scope of this study.

Evaluation of cloud layer origin in multilayer profiles indicates that more than half (55%) of all multilayer profiles include cloud layers associated with more than one cluster, suggesting differing sources and differential advection as a function of height. Moreover, even if both warm moist advection clusters (1 and 2) are treated as comparable sources, more than 2 in every 5 multilayer profiles still contain cloud layers with markedly different air mass source properties, for example, a combination of Clusters 1 and 4 in clouds observed in the same profiles. These results imply that detailed case studies focusing on the formation and evolution of Eulerian multilayer cloud observations (or at the very least based on the MOSAiC observations) should be performed with the required knowledge of possibly differing overlying cloudy air mass sources, to prevent mishandling of observational benchmarks.

Analysis of relative changes in air mass moisture over sea ice ($\widetilde{\Delta q_v}$ depicted in **Figure 2b**) underscores the importance of air mass moistening via some mixing with water vapor originating in open water patches and ice leads, even in the case of the air masses confined to extensively covered sea-ice regions (Cluster 4). Thus, some of the cloud observations associated with Cluster 4 could insinuate a local role of ice leads in the formation of clouds and maintenance of some moisture in the air masses. The $\overline{z/PBLH}$ analysis (**Figure 2c**) shows that approximately two thirds of Cluster 4's air masses could be moistened via some degree of interaction with the surface while noting that this fraction value could vary to some extent as a result of the PBLH diagnostic uncertainty discussed above.

About one third of the air masses grouped into Cluster 4, representing approximately 7% of the trajectory data set, do not show indications of surface coupling. These free-atmosphere air masses typically exhibit neutral to weak subsidence of up to approximately 0.2 cm/s (not shown) when examined up to a few or 24 h prior to the MOSAiC overpass, or since the last open water overpass (for reference, the full air mass back-trajectory data set demonstrates comparable mean upward motions of 0.2–0.3 cm/s). Therefore, cloud formation via a weak ascent of subsaturated air masses is also not a likely mechanism for the formation of these cluster 4 clouds. Because these

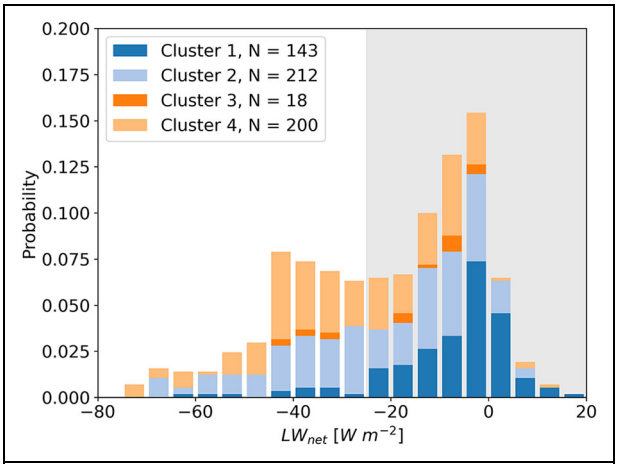

Figure 6. Net surface longwave radiation (LW_{net}) histograms for each cluster based on measurements from the MOSAiC central observatory (see legend; bin width of 5 W m^{-2}). The histograms are calculated for cloud-bearing profiles in which all the detected clouds are associated with a single cluster. The number of samples (*N*) in each cluster histogram is provided in the legend. The shaded area designates the "radiatively cloudy" state, determined based on LW_{net} histogram for the full deployment data (Figure S2). DOI: https://doi.org/10.1525/elementa.2021.000071.f6

circulating Arctic air masses ultimately formed the observed cloud layers over MOSAiC without advection of moist air and/or weak ascent serving as the cloud inception mechanisms, we conclude that these clouds were fundamentally formed via persistent radiative cooling of elevated (stable and stratified) initially subsaturated air masses (e.g., Simpfendoerfer et al., 2019). Considering the prolonged periods during which some Cluster 2's air masses are advected over non–open water surface (**Figure 2a** and **d**) and the large fraction of seemingly decoupled cases associated with this cluster as well as the decoupled state of all of Cluster 3's air masses (**Figure 2c**), it is possible that this formation mechanism is rather frequent, responsible for up to 1 of every 5 detected cloud layers.

A follow-up question concerning this potentially common Arctic cloud formation mechanism is whether the ensuing clouds could be radiatively important for the surface energy budget. (We note that an equivalent question concerning the importance of these clouds for the atmospheric thermodynamic profile warrants future dedicated studies.) **Figure 6** illustrates net surface longwave radiation (LW_{net}) histograms corresponding to each of the 4 clusters in cloud-bearing profiles in which all detected clouds are associated with a single cluster. The histograms are based on quality-controlled surface radiation measurements made commensurate with the sounding and remote-sensing measurements at the MOSAiC central observatory. We use the primary radiation measurements made at the "Met City" location by the DOE Atmospheric Radiation Measurement Program from October 16, 2019, to May 7, 2020, and June 28, 2020, to July 14, 2020. Additionally, measurements made by 2 Atmospheric Surface Flux Stations (ASFS) were included to provide as complete a record as possible: ASFS30 between May 8 to May 18, 2020, June 16 to June 27, 2020, and August 22 to September 20, 2020, and ASFS50 from July 15 to July 30, 2020. Measurements from these different instrument suites were cross-validated and demonstrated high consistency (not shown). The available LW_{net} measurements are averaged in 15-min windows following radiosonde release times, thereby covering the radiosonde ascent up to approximately 4.3 km (cf. Silber et al., 2021a), making these averaged samples well correspondent with the vast majority of detected cloud layers (**Figure 3c**). Note that we assume radiative uniformity over these time scales across the LW_{net} measurement suites and between these suites and the radiosonde launches from onboard *Polarstern* (all within a few hundred meters of each other). As a qualitative metric for the radiative importance of the clouds, we use the LW_{net} "radiatively cloudy" state (shaded area in **Figure 6**; e.g., Stramler et al., 2011). The lower threshold of the "radiatively cloudy" state is set at −25 W m^{-2} based on the local minima in the full deployment's LW_{net} histogram (Figure S2; cf. Stramler et al., 2011; Cesana et al., 2012; Pithan et al., 2014; Silber et al., 2019a).

As demonstrated in **Figure 6**, the vast majority (92%) of Cluster 1 cloudy air masses are associated with the "radiatively cloudy" conditions at the central observatory, whereas most Cluster 2 and 3 cases (56% and 67%, respectively) are also associated with the "radiatively cloudy" state, but with a significant percentage of cases in which "radiatively clear" surface conditions are measured.

Cluster 4, wherein clouds are most likely to have formed via the radiative cooling of elevated stable air masses, shows a rather balanced occurrence of the two radiative states, with 44% of cases being within the "radiatively cloudy" state. The Cluster 4 clouds exhibiting a "radiatively clear" signature would need to be tenuous (i.e., little condensed liquid water) and/or elevated clouds, which are typically colder relative to the surface. Since most Cluster 4 clouds occur at low levels (**Figure 3c**), the "radiatively-clear" conditions in this cluster are primarily the product of optically thin clouds, as supported by small liquid water paths derived from microwave radiometer measurements (not shown). These clouds are nonetheless more likely to induce a positive net surface radiation when the solar zenith angle is below 90° (e.g., Turner et al., 2007; Bennartz et al., 2013). Moreover, the early life cycle stages of polar clouds generated via this formation mechanism, prior to cloud-induced turbulence onset and significant optical thickening, can persist for extended periods (e.g., Silber et al., 2020), especially at limited droplet number concentrations common to the central Arctic region (e.g., Mauritsen et al., 2011) and lesser temperatures (see Silber et al., 2020). Thus, many of the "radiatively clear" clouds in Cluster 4 could be at a stage before, or after, significant liquid water formation during which time their peak radiative impact occurs.

A qualitative evaluation of the radiative significance of Cluster 4's likely decoupled clouds ($\overline{z/\mathrm{PBLH}} \geq 5$) can be made by examining a total of 67 samples of cloud-bearing profiles consisting of only Cluster 4 clouds, which coincide

with this $\overline{z/\mathrm{PBLH}}$ criterion. We find that approximately 1 of 2 decoupled cloud-bearing profiles associated only with Cluster 4 is within the "radiatively cloudy" state, with 4.5% of these profiles even resulting in net longwave warming of the surface. These results provide a lower limit to the radiative significance of these clouds and suggest that the formation of cloud layers via persistent radiative cooling of stable Arctic air masses can frequently impact the surface energy budget once the formed cloud becomes optically thick (e.g., Simpfendoerfer et al., 2019; Silber et al., 2020).

5. Summary

Understanding Arctic cloud life cycles requires knowledge about their air mass origin and characteristics. Here, we analyzed back-trajectory calculations for liquid-bearing cloud layers detected in the MOSAiC field campaign sounding data set to better understand the sources of air masses that support central Arctic cloud formation. We used a unique set of 4 air mass back-trajectory variables to cluster this trajectory data set, resulting in a robust product that largely separates these trajectory source regions into the ice-covered Arctic, mid- to high-latitude coastal and continental or open water regions, and low- to midlatitude open water regions. By scrutinizing this analysis, we find that:

- Warm moist air intrusions into the central Arctic typically result in multilayer liquid-bearing cloud structures with a large number of overlying layers.
- Multiple liquid-bearing cloud layers are detected in half of the examined atmospheric profiles containing liquid-bearing clouds, with profiles of at least 4 overlying cloud layers occurring in approximately 16% of all cloud-bearing profiles.
- More than half of all multilayer profiles include cloud layers associated with different sources, suggesting that studies based on Eulerian multilayer liquid-bearing cloud observations should be performed with knowledge of cloudy air mass trajectories and source regions to prevent mishandling of observational targets.
- Two thirds of the clouds observed over MOSAiC that were associated with Arctic air circulating over high sea-ice concentration regions (Cluster 4) were likely partially induced or augmented by open water patches and ice leads that moistened the associated air masses.
- Arctic cloud formation via persistent radiative cooling of elevated stable subsaturated air masses can occur frequently (up to 1 of 5 cloud cases in the MOSAiC sounding data set) and may lead to a substantial cloud radiative impact on the surface.

The Lagrangian analysis presented here provides a basis for further investigations into cloudiness observed during MOSAiC and offers context for evaluations of how representative the MOSAiC observations are of the current state of the central Arctic. While the air mass back-trajectory data set is local to the MOSAiC deployment, it could be useful for detailed case studies not only focusing on the MOSAiC deployment but also for studies examining Arctic cloud physics from a general Lagrangian perspective (see also Ali and Pithan, 2020). Such studies can offer key insight into processes involved in air mass evolution, cloud persistence, and the net cloud impact on the Arctic system.

Data accessibility statement

Radiosonde data were obtained through a partnership between the Alfred Wegener Institute (AWI), the Atmospheric Radiation Measurement (ARM) User Facility, U.S. Department of Energy facility managed by the Biological and Environmental Research Program, and the German Weather Service (DWD), and are available from the PANGAEA archive (Maturilli et al., 2021). Surface radiation measurements are from 2 sources: the ARM User Facility (Riihimaki, 2021) and the University of Colorado/NOAA surface flux team, available at the Arctic Data Center (Cox et al., 2021a; Cox et al., 2021b). ERA5 reanalysis data are available at the Copernicus Climate Data Store (https://climate.copernicus.eu/climate-reanalysis). The HSRL liquid cloud base height data product for the MOSAiC deployment is available on the ARM Archive (Silber et al., 2021b). The back-trajectory data set is available on the ARM data archive under DOI: http://dx.doi.org/10.5439/1840519.

Supplemental files

The supplemental files for this article can be found as follows:

Figures S1 and S2. PDF

Acknowledgments

Measurements used in this manuscript were collected as part of the international Multidisciplinary drifting Observatory for the Study of the Arctic Climate (MOSAiC) with the tag MOSAiC20192020 and the Project_ID: AWI_PS122_00. We thank the large team responsible for collecting the MOSAiC radiosonde data set.

Funding

This research was supported by the U.S. Department of Energy Atmospheric System Research Program under grants DE-SC0021004 and DE-SC0021341.

Competing interests

MDS serves as a guest editor for Elementa but has served no editorial role for this manuscript.

Author contributions

- Conceptualization, design, formal analysis, and manuscript preparation: IS.
- Acquisition of data: IS, MDS.
- Critical review of the manuscript: MDS.
- Final approval of the versions to be submitted: IS and MDS.

References

Ali, SM, Pithan, F. 2020. Following moist intrusions into the Arctic using SHEBA observations in a Lagrangian perspective. *Quarterly Journal of the Royal Meteorological Society* **146**(732): 3522–3533. DOI: http://dx.doi.org/10.1002/qj.3859.

Attias, H. 2000. A variational Bayesian framework for graphical models, in *Advances in neural information processing systems;* Vol. **12**. Cambridge, MA: MIT Press: 209–215.

Bambha, R, Eloranta, E, Garcia, J, Michelsen, H, Goldsmith, J, Ermold, B. 2019. High Spectral Resolution Lidar (HSRL). *Atmospheric Radiation Measurement (ARM) User Facility*. DOI: http://dx.doi.org/10.5439/1025200.

Bennartz, R, Shupe, MD, Turner, DD, Walden, VP, Steffen, K, Cox, CJ, Kulie, MS, Miller, NB, Pettersen, C. 2013. July 2012 Greenland melt extent enhanced by low-level liquid clouds. *Nature* **496**(7443): 83–86. DOI: http://dx.doi.org/10.1038/nature12002.

Binder, H, Boettcher, M, Grams, CM, Joos, H, Pfahl, S, Wernli, H. 2017. Exceptional air mass transport and dynamical drivers of an extreme wintertime arctic warm event. *Geophysical Research Letters* **44**(23): 12–28, 36. DOI: http://dx.doi.org/10.1002/2017GL075841.

Blei, DM, Jordan, MI. 2006. Variational inference for Dirichlet process mixtures. *Bayesian Analysis* **1**(1): 121–143. DOI: http://dx.doi.org/10.1214/06-BA104.

Boisvert, LN, Wu, DL, Shie, C-L. 2015. Increasing evaporation amounts seen in the Arctic between 2003 and 2013 from AIRS data. *Journal of Geophysical Research: Atmospheres* **120**(14): 6865–6881. DOI: http://dx.doi.org/10.1002/2015JD023258.

Cesana, G, Kay, JE, Chepfer, H, English, JM, de Boer, G. 2012. Ubiquitous low-level liquid-containing Arctic clouds: New observations and climate model constraints from CALIPSO-GOCCP. *Geophysical Research Letters* **39**(20). DOI: http://dx.doi.org/10.1029/2012GL053385.

Chen, Y-S, Harrington, JY, Verlinde, J, Zhang, F, Oue, M. 2020. Dynamical response of an arctic mixed-phase cloud to ice precipitation and Downwelling Longwave radiation from an upper-level cloud. *Journal of Geophysical Research: Atmospheres* **125**(2): e2019JD031089. DOI: http://dx.doi.org/10.1029/2019JD031089.

Cox, C, Gallagher, M, Shupe, M, Persson, O, Solomon, A, Ayers, T, Costa, D, Hutchings, J, Leach, J, Morris, S, Osborn, J, Pezoa, S, Uttal, T. 2021a. Atmospheric Surface Flux Station #30 measurements (Level 1 Raw), Multidisciplinary Drifting Observatory for the Study of Arctic Climate (MOSAiC), central Arctic, October 2019 - September 2020. Arctic Data Center. DOI: http://dx.doi.org/10.18739/A20C4SM1J.

Cox, C, Gallagher, M, Shupe, M, Persson, O, Solomon, A, Ayers, T, Costa, D, Hutchings, J, Leach, J, Morris, S, Osborn, J, Pezoa, S, Uttal, T. 2021b. Atmospheric Surface Flux Station #50 measurements (Level 1 Raw), Multidisciplinary Drifting Observatory for the Study of Arctic Climate (MOSAiC), central Arctic, October 2019 - September 2020. Arctic Data Center. DOI: http://dx.doi.org/10.18739/A2445HD46.

Cox, CJ, Uttal, T, Long, CN, Shupe, MD, Stone, RS, Starkweather, S. 2016. The role of springtime Arctic clouds in determining autumn sea ice extent. *Journal of Climate* **29**(18): 6581–6596. DOI: http://dx.doi.org/10.1175/JCLI-D-16-0136.1.

Curry, JA. 1983. On the formation of continental polar air. *Journal of the Atmospheric Sciences* **40**(9): 2278–2292. DOI: http://dx.doi.org/10.1175/1520-0469(1983)040<2278:OTFOCP>2.0.CO;2.

Curry, JA, Schramm, JL, Rossow, WB, Randall, D. 1996. Overview of arctic cloud and radiation characteristics. *Journal of Climate* **9**(8): 1731–1764. DOI: http://dx.doi.org/10.1175/1520-0442(1996)009<1731:OOACAR>2.0.CO;2

Dong, X, Xi, B, Crosby, K, Long, CN, Stone, RS, Shupe, MD. 2010. A 10 year climatology of Arctic cloud fraction and radiative forcing at Barrow, Alaska. *Journal of Geophysical Research: Atmospheres* **115**(D17). DOI: http://dx.doi.org/10.1029/2009JD013489.

Donlon, CJ, Martin, M, Stark, J, Roberts-Jones, J, Fiedler, E, Wimmer, W. 2012. The operational sea surface temperature and sea ice analysis (OSTIA) system. *Remote Sensing of Environment* **116**: 140–158. DOI: http://dx.doi.org/10.1016/j.rse.2010.10.017.

Doyle, JG, Lesins, G, Thackray, CP, Perro, C, Nott, GJ, Duck, TJ, Damoah, R, Drummond, JR. 2011. Water vapor intrusions into the High Arctic during winter. *Geophysical Research Letters* **38**(12). DOI: http://dx.doi.org/10.1029/2011GL047493.

ECMWF. 2016. Part IV: Physical processes, in *IFS Documentation CY41R2. ECMWF*. Available at https://www.ecmwf.int/node/16648.

Eloranta, EW. 2005. High spectral resolution lidar, in Weitkamp, C ed., *Lidar: Range-resolved optical remote sensing of the atmosphere*. New York, NY: Springer: 143–163.

Fearon, MG, Doyle, JD, Ryglicki, DR, Finocchio, PM, Sprenger, M. 2021. The role of cyclones in moisture transport into the arctic. *Geophysical Research Letters* **48**(4): e2020GL090353. DDOI: http://dx.doi.org/10.1029/2020GL090353.

Garrett, TJ, Maestas, MM, Krueger, SK, Schmidt, CT. 2009. Acceleration by aerosol of a radiative-thermodynamic cloud feedback influencing Arctic surface warming. *Geophysical Research Letters* **36**(19). DOI: http://dx.doi.org/10.1029/2009GL040195.

Gimeno, L, Vázquez, M, Eiras-Barca, J, Sorí, R, Algarra, I, Nieto, R. 2019. Atmospheric moisture transport and the decline in Arctic Sea ice. *WIREs Climate Change* **10**(4): e588. DOI: http://dx.doi.org/10.1002/wcc.588.

Graham, RM, Cohen, L, Ritzhaupt, N, Segger, B, Graversen, RG, Rinke, A, Walden, VP, Granskog, MA, Hudson, SR. 2019a. Evaluation of six atmospheric reanalyses over Arctic sea ice from winter to early summer. *Journal of Climate* **32**(14): 4121–4143. DOI: http://dx.doi.org/10.1175/JCLI-D-18-0643.1.

Graham, RM, Hudson, SR, Maturilli, M. 2019b. Improved performance of ERA5 in Arctic gateway relative to four global atmospheric reanalyses. *Geophysical Research Letters* **46**(11): 6138–6147. DOI: http://dx.doi.org/10.1029/2019GL082781.

Gu, M, Wang, Z, Wei, J, Yu, X. 2021. An assessment of Arctic cloud water paths in atmospheric reanalyses. *Acta Oceanologica Sinica* **40**(3): 46–57. DOI: http://dx.doi.org/10.1007/s13131-021-1706-5.

Herman, G, Goody, R. 1976. Formation and persistence of summertime arctic stratus clouds. *Journal of the Atmospheric Sciences* **33**(8): 1537–1553. DOI: http://dx.doi.org/10.1175/1520-0469(1976)033<1537:FAPOSA>2.0.CO;2.

Hersbach, H, Bell, B, Berrisford, P, Hirahara, S, Horányi, A, Muñoz-Sabater, J, Nicolas, J, Peubey, C, Radu, R, Schepers, D, Simmons, A. 2020. The ERA5 global reanalysis. *Quarterly Journal of the Royal Meteorological Society* **146**(730): 1999–2049. DOI: http://dx.doi.org/10.1002/qj.3803.

Hirahara, S, Balmaseda, MA, de Boisseson, E, Hersbach, H 2016 *Sea surface temperature and sea ice concentration for ERA5. Eur. Berkshire, UK: Centre Medium Range Weather Forecasts* ERA Rep. Ser (Vol. **26**).

Hodges, JL. 1958. The significance probability of the Smirnov two-sample test. *Arkiv För Matematik* **3**(5): 469–486.

Holdridge, D. 2020. *Balloon-borne sounding system (SONDE) instrument handbook*. ARM-TR-029, DOE Office of Science, Office of Biological and Environmental Research. DOI: http://dx.doi.org/10.2172/1020712.

Intrieri, JM, Shupe, MD, Uttal, T, McCarty, BJ 2002. An annual cycle of Arctic cloud characteristics observed by radar and lidar at SHEBA. *Journal of Geophysical Research* **107**(C10): 8030. DOI: http://dx.doi.org/10.1029/2000JC000423.

Jakobson, E, Vihma, T. 2010. Atmospheric moisture budget in the Arctic based on the ERA-40 reanalysis. *International Journal of Climatology* **30**(14): 2175–2194. DOI: http://dx.doi.org/10.1002/joc.2039.

Kay, JE, Gettelman, A. 2009. Cloud influence on and response to seasonal Arctic sea ice loss. *Journal of Geophysical Research: Atmospheres* **114**(D18). DOI: http://dx.doi.org/10.1029/2009JD011773.

Kay, JE, L'Ecuyer, T, Chepfer, H, Loeb, N, Morrison, A, Cesana, G. 2016. Recent advances in arctic cloud and climate research. *Current Climate Change Reports* **2**(4): 159–169. DOI: http://dx.doi.org/10.1007/s40641-016-0051-9.

Kay, JE, L'Ecuyer, T, Gettelman, A, Stephens, G, O'Dell, C.2008The contribution of cloud and radiation anomalies to the 2007 Arctic sea ice extent minimum. *Geophysical Research Letters* **35**(8). DOI: http://dx.doi.org/10.1029/2008GL033451.

Kay, JE, Raeder, K, Gettelman, A, Anderson, J. 2011. The boundary layer response to recent Arctic sea ice loss and implications for high-latitude climate feedbacks. *Journal of Climate* **24**(2): 428–447. DOI: http://dx.doi.org/10.1175/2010JCLI3651.1.

Läderach, A, Sodemann, H. 2016. A revised picture of the atmospheric moisture residence time. *Geophysical Research Letters* **43**(2): 924–933. DOI: http://dx.doi.org/10.1002/2015GL067449.

Lenaerts, JTM, Van Tricht, K, Lhermitte, S, L'Ecuyer, TS. 2017. Polar clouds and radiation in satellite observations, reanalyses, and climate models. *Geophysical Research Letters* **44**(7): 3355–3364. DOI: http://dx.doi.org/10.1002/2016GL072242.

Li, X, Krueger, SK, Strong, C, Mace, GG, Benson, S. 2020. Midwinter Arctic leads form and dissipate low clouds. *Nature Communications* **11**(1): 206. DOI: http://dx.doi.org/10.1038/s41467-019-14074-5.

Liu, C, Barnes, EA. 2015. Extreme moisture transport into the Arctic linked to Rossby wave breaking. *Journal of Geophysical Research: Atmospheres* **120**(9): 3774–3788. DOI: https://doi.org/10.1002/2014JD022796.

Maturilli, M, Holdridge, DJ, Dahlke, S, Graeser, J, Sommerfeld, A, Jaiser, R, Deckelmann, H, Schulz, A. 2021. Initial radiosonde data from 2019-10 to 2020-09 during project MOSAiC. PANGAEA. DOI: http://dx.doi.org/10.1594/PANGAEA.928656.

Mauritsen, T, Sedlar, J, Tjernström, M, Leck, C, Martin, M, Shupe, M, Sjogren, S, Sierau, B, Persson, PO, Brooks, IM, Swietlicki, E. 2011. An Arctic CCN-limited cloud-aerosol regime. *Atmospheric Chemistry and Physics* **11**(1): 165–173. DOI: http://dx.doi.org/10.5194/acp-11-165-2011.

Miller, NB, Shupe, MD, Cox, CJ, Walden, VP, Turner, DD, Steffen, K. 2015. Cloud radiative forcing at summit, Greenland. *Journal of Climate* **28**(15): 6267–6280. DOI: http://dx.doi.org/10.1175/JCLI-D-15-0076.1.

Naakka, T, Nygård, T, Vihma, T, Sedlar, J, Graversen, R. 2019. Atmospheric moisture transport between mid-latitudes and the Arctic: Regional, seasonal and vertical distributions. *International Journal of Climatology* **39**(6): 2862–2879. DOI: http://dx.doi.org/10.1002/joc.5988.

Nicolas, JP, Vogelmann, AM, Scott, RC, Wilson, AB, Cadeddu, MP, Bromwich, DH, Verlinde, J, Lubin, D, Russell, LM, Jenkinson, C, Powers, HH. 2017. January 2016 extensive summer melt in West Antarctica favoured by strong El Niño. *Nature Communications* **8**: 15799. DOI: http://dx.doi.org/10.1038/ncomms15799.

Nygård, T, Naakka, T, Vihma, T. 2020. Horizontal moisture transport dominates the regional moistening patterns in the Arctic. *Journal of Climate* **33**(16): 6793–6807. DOI: http://dx.doi.org/10.1175/JCLI-D-19-0891.1.

Papritz, L, Dunn-Sigouin, E. 2020. What configuration of the atmospheric circulation drives extreme net and

total moisture transport into the Arctic. *Geophysical Research Letters* **47**(17): e2020GL089769. DOI: http://dx.doi.org/10.1029/2020GL089769.

Pedregosa, F, Varoquaux, G, Gramfort, A, Michel, V, Thirion, B, Grisel, O, Blondel, M, Prettenhofer, P, Weiss, R, Dubourg, V, Vanderplas, J. 2011. Scikit-learn: Machine learning in python. *Journal of Machine Learning Research* **12**(85): 2825–2830. http://jmlr.org/papers/v12/pedregosa11a.html.

Persson, POG. 2012. Onset and end of the summer melt season over sea ice: Thermal structure and surface energy perspective from SHEBA. *Climate Dynamics* **39**(6): 1349–1371. DOI: http://dx.doi.org/10.1007/s00382-011-1196-9.

Pinto, JO, Alam, A, Maslanik, JA, Curry, JA, Stone, RS. 2003. Surface characteristics and atmospheric footprint of springtime Arctic leads at SHEBA. *Journal of Geophysical Research: Oceans* **108**(C4). DOI: http://dx.doi.org/10.1029/2000JC000473.

Pithan, F, Medeiros, B, Mauritsen, T. 2014. Mixed-phase clouds cause climate model biases in Arctic wintertime temperature inversions. *Climate Dynamics* **43**(1): 289–303. DOI: http://dx.doi.org/10.1007/s00382-013-1964-9.

Pithan, F, Svensson, G, Caballero, R, Chechin, D, Cronin, TW, Ekman, AML, Neggers, R, Shupe, MD, Solomon, A, Tjernström, M, Wendisch, M. 2018. Role of air-mass transformations in exchange between the Arctic and mid-latitudes. *Nature Geoscience* **11**(11): 805–812. DOI: http://dx.doi.org/10.1038/s41561-018-0234-1.

Renfrew, IA, Barrell, C, Elvidge, AD, Brooke, JK, Duscha, C, King, JC, Kristiansen, J, Cope, TL, Moore, GW, Pickart, RS, Reuder, J. 2021. An evaluation of surface meteorology and fluxes over the Iceland and Greenland Seas in ERA5 reanalysis: The impact of sea ice distribution. *Quarterly Journal of the Royal Meteorological Society* **147**(734): 691–712. DOI: http://dx.doi.org/10.1002/qj.3941.

Riihimaki, L. 2021. Radiation instruments on ice (ICERADRIIHIMAKI). *Atmospheric Radiation Measurement (ARM) User Facility*. DOI: http://dx.doi.org/10.5439/1608608.

Rinke, A, Segger, B, Crewell, S, Maturilli, M, Naakka, T, Nygård, T, Vihma, T, Alshawaf, F, Dick, G, Wickert, J, Keller, J. 2019. Trends of vertically integrated water vapor over the Arctic during 1979–2016: Consistent moistening all over? *Journal of Climate* **32**(18): 6097–6116. DOI: http://dx.doi.org/10.1175/JCLI-D-19-0092.1.

Rousseeuw, PJ. 1987. Silhouettes: A graphical aid to the interpretation and validation of cluster analysis. *Journal of Computational and Applied Mathematics* **20**: 53–65. DOI: http://dx.doi.org/10.1016/0377-0427(87)90125-7.

Schweiger, A J, Lindsay, RW, Vavrus, S, Francis, JA. 2008. Relationships between Arctic sea ice and clouds during autumn. *Journal of Climate* **21**(18): 4799–4810. DOI: http://dx.doi.org/10.1175/2008JCLI2156.1.

Seidel, DJ, Zhang, Y, Beljaars, A, Golaz, J-C, Jacobson, AR, Medeiros, B. 2012. Climatology of the planetary boundary layer over the continental United States and Europe. *Journal of Geophysical Research: Atmospheres* **117** (D17). DOI: http://dx.doi.org/10.1029/2012JD018143.

Serreze, MC, Barry, RG. 1988. Synoptic activity in the Arctic Basin, 1979–85. *Journal of Climate* **1**(12): 1276–1295. DOI: http://dx.doi.org/10.1175/1520-0442(1988)001<1276:SAITAB>2.0.CO;2.

Shupe, MD. 2011. Clouds at Arctic atmospheric observatories. Part II: Thermodynamic phase characteristics. *Journal of Applied Meteorology and Climatology* **50**(3): 645–661. DOI: http://dx.doi.org/10.1175/2010JAMC2468.1.

Shupe, MD, Intrieri, JM. 2004. Cloud radiative forcing of the arctic surface: The influence of cloud properties, surface Albedo, and Solar Zenith Angle. *Journal of Climate* **17**(3): 616–628. DOI: http://dx.doi.org/10.1175/1520-0442(2004)017<0616:CRFOTA>2.0.CO;2.

Shupe, MD, Matrosov, SY, Uttal, T. 2006. Arctic mixed-phase cloud properties derived from surface-based sensors at SHEBA. *Journal of the Atmospheric Sciences* **63**(2): 697–711.

Shupe, MD, Rex, M, Blomquist, B, Persson, POG, Schmale, J, Uttal, T, Althausen, D, Angot, H, Archer, S, Bariteau, L, Beck, I. 2021. Overview of the MOSAiC expedition—Atmosphere. *Elementa: Science of the Anthropocene* **10**(1). DOI: http://dx.doi.org/10.1525/elementa.2021.00060.

Shupe, MD, Rex, M, Dethloff, K, Damm, E, Fong, AA, Gradinger, R, Heuzé, C, Loose, B, Makarov, A, Maslowski, W, Nicolaus, M. 2020. *The MOSAiC expedition: A year drifting with the Arctic sea ice*, in Thoman, RL, Richter-Menge, J, Druckenmiller, ML eds., *Arctic report card 2020*. DOI: http://dx.doi.org/10.25923/9g3v-xh92.

Shupe, MD, Walden, VP, Eloranta, E, Uttal, T, Campbell, JR, Starkweather, SM, Shiobara, M. 2011. Clouds at Arctic atmospheric observatories. Part I: Occurrence and macrophysical properties. *Journal of Applied Meteorology and Climatology* **50**(3): 626–644. DDOI: http://dx.doi.org/10.1175/2010JAMC2467.1

Silber, I, Fridlind, AM, Verlinde, J, Ackerman, AS, Cesana, GV, Knopf, DA. 2021a. The prevalence of precipitation from polar supercooled clouds. *Atmospheric Chemistry and Physics*. DOI: http://dx.doi.org/10.5194/acp-21-3949-2021.

Silber, I, Fridlind, AM, Verlinde, J, Russell, LM, Ackerman, AS. 2020. Nonturbulent liquid-bearing polar clouds: observed frequency of occurrence and simulated sensitivity to gravity waves. *Geophysical Research Letters*. DOI: http://dx.doi.org/10.1029/2020GL087099.

Silber, I, Verlinde, J, Cadeddu, M, Flynn, CJ, Vogelmann, AM, Eloranta, EW. 2019a. Antarctic cloud macrophysical, thermodynamic phase, and atmospheric inversion coupling properties at McMurdo Station. Part II: Radiative impact during different synoptic regimes. *Journal of Geophysical Research:*

Atmospheres. DOI: http://dx.doi.org/10.1029/2018JD029471.

Silber, I, Verlinde, J, Eloranta, EW. 2021b. HSRL Liquid cloud base height. United States. DOI: http://dx.doi.org/10.5439/1764692.

Silber, I, Verlinde, J, Eloranta, EW, Flynn, CJ, Flynn, DM. 2018. Polar liquid cloud base detection algorithms for high spectral resolution or micropulse lidar data. *Journal of Geophysical Research: Atmospheres*. DOI: http://dx.doi.org/10.1029/2017JD027840.

Silber, I, Verlinde, J, Wang, S-H, Bromwich, DH, Fridlind, AM, Cadeddu, M, Eloranta, EW. 2019b. Cloud influence on ERA5 and AMPS surface downwelling longwave radiation biases in West Antarctica. *Journal of Climate*. DOI: http://dx.doi.org/10.1175/JCLI-D-19-0149.1.

Simmonds, I, Burke, C, Keay, K. 2008. Arctic climate change as manifest in cyclone behavior. *Journal of Climate* **21**(22): 5777–5796. DOI: http://dx.doi.org/10.1175/2008JCLI2366.1.

Simpfendoerfer, LF, Verlinde, J, Harrington, JY, Shupe, MD, Chen, Y-S, Clothiaux, EE, Golaz, J-C. 2019. Formation of Arctic stratocumuli through atmospheric radiative cooling. *Journal of Geophysical Research: Atmospheres*. DOI: http://dx.doi.org/10.1029/2018JD030189.

Stein, AF, Draxler, RR, Rolph, GD, Stunder, BJB, Cohen, MD, Ngan, F. 2015. NOAA's HYSPLIT atmospheric transport and dispersion modeling system. *Bulletin of the American Meteorological Society* **96**(12): 2059–2077. DOI: http://dx.doi.org/10.1175/BAMS-D-14-00110.1.

Stramler, K, Del Genio, AD, Rossow, WB. 2011. Synoptically driven arctic winter states. *Journal of Climate* **24**(6): 1747–1762. DOI: http://dx.doi.org/10.1175/2010JCLI3817.1.

Tan, I, Storelvmo, T. 2019. Evidence of strong contributions from mixed-phase clouds to Arctic climate change. *Geophysical Research Letters* **46**(5): 2894–2902. DOI: http://dx.doi.org/10.1029/2018GL081871.

Tjernström, M, Shupe, MD, Brooks, IM, Achtert, P, Prytherch, J, Sedlar, J. 2019. Arctic summer airmass transformation, surface inversions, and the surface energy budget. *Journal of Climate* **32**(3): 769–789.

Tjernström, M, Shupe, MD, Brooks, IM, Persson, POG, Prytherch, J, Salisbury, DJ, Sedlar, J, Achtert, P, Brooks, BJ, Johnston, PE, Sotiropoulou, G. 2015. Warm-air advection, air mass transformation and fog causes rapid ice melt. *Geophysical Research Letters* **42**(13): 5594–5602. DOI: http://dx.doi.org/10.1002/2015GL064373.

Turner, DD, Shupe, MD, Zwink, AB. 2018. Characteristic atmospheric radiative heating rate profiles in Arctic clouds as observed at barrow, Alaska. *Journal of Applied Meteorology and Climatology* **57**(4): 953–968. DOI: http://dx.doi.org/10.1175/JAMC-D-17-0252.1.

Turner, DD, Vogelmann, AM, Johnson, K, Miller, M, Austin, RT, Barnard, JC, Cady-Pereira, K, Chiu, JC, Clough, SA, Flynn, C, Khaiyer, MM, Liljegren, J, Johnson, K. 2007. Thin liquid water clouds: Their importance and our challenge. *Bulletin of the American Meteorological Society* **88**(2): 177–190. DOI: http://dx.doi.org/10.1175/BAMS-88-2-177.

Uttal, T, Curry, JA, McPhee, MG, Perovich, DK, Moritz, RE, Maslanik, JA, Guest, PS, Stern, HL, Moore, JA, Turenne, R, Heiberg, A. 2002. Surface heat budget of the Arctic Ocean. *Bulletin of the American Meteorological Society* **83**(2): 255–276. DOI: http://dx.doi.org/10.1175/1520-0477(2002)083<0255:SHBOTA>2.3.CO;2.

van der Ent, RJ, Tuinenburg, OA. 2017. The residence time of water in the atmosphere revisited. *Hydrology and Earth System Sciences* **21**(2): 779–790. DOI: http://dx.doi.org/10.5194/hess-21-779-2017.

Van Tricht, K, Lhermitte, S, Lenaerts, JTM, Gorodetskaya, IV, L'Ecuyer, TS, Noël, B, van den Broeke, MR, Turner, DD, van Lipzig, NP. 2016. Clouds enhance Greenland ice sheet meltwater runoff. *Nature Communications* **7**: 10266. DOI: http://dx.doi.org/10.1038/ncomms10266.

Vázquez, M, Nieto, R, Drumond, A, Gimeno, L. 2016. Moisture transport into the Arctic: Source-receptor relationships and the roles of atmospheric circulation and evaporation. *Journal of Geophysical Research: Atmospheres* **121**(22): 13, 413–493, 509. DOI: http://dx.doi.org/10.1002/2016JD025400.

Verlinde, J, Rambukkange, MP, Clothiaux, EE, McFarquhar, GM, Eloranta, EW. 2013. Arctic multilayered, mixed-phase cloud processes revealed in millimeter-wave cloud radar Doppler spectra. *Journal of Geophysical Research: Atmospheres* **118**(23): 13, 199–13, 213. DOI: http://dx.doi.org/10.1002/2013JD020183.

Vogelezang, DHP, Holtslag, AAM. 1996. Evaluation and model impacts of alternative boundary-layer height formulations. *Boundary-Layer Meteorology* **81**(3): 245–269. DOI: http://dx.doi.org/10.1007/BF02430331.

Woods, C, Caballero, R. 2016. The role of moist intrusions in winter Arctic warming and sea ice decline. *Journal of Climate* **29**(12): 4473–4485. DOI: http://dx.doi.org/10.1175/JCLI-D-15-0773.1.

Woods, C, Caballero, R, Svensson, G. 2013. Large-scale circulation associated with moisture intrusions into the Arctic during winter. *Geophysical Research Letters* **40**(17): 4717–4721. DOI: http://dx.doi.org/10.1002/grl.50912.

Yao, B, Teng, S, Lai, R, Xu, X, Yin, Y, Shi, C, Liu, C. 2020. Can atmospheric reanalyses (CRA and ERA5) represent cloud spatiotemporal characteristics? *Atmospheric Research* **244**: 105091. DOI: http://dx.doi.org/10.1016/j.atmosres.2020.105091.

You, C, Tjernström, M, Devasthale, A. 2021. Eulerian and Lagrangian views of warm and moist air intrusions into summer Arctic. *Atmospheric Research* **256**: 105586. DOI: http://dx.doi.org/10.1016/j.atmosres.2021.105586.

Zulauf, MA, Krueger, SK. 2003. Two-dimensional numerical simulations of Arctic leads: Plume penetration height. *Journal of Geophysical Research: Oceans* **108**(C2). DOI: http://dx.doi.org/10.1029/2000JC000495.

How to cite this article: Silber, I, Shupe, MD. 2022. Insights on sources and formation mechanisms of liquid-bearing clouds over MOSAiC examined from a Lagrangian framework. *Elementa: Science of the Anthropocene* 10(1). DOI: https://doi.org/10.1525/elementa.2021.000071

Domain Editor-in-Chief: Detlev Helmig, Boulder AIR LLC, Boulder, CO, USA

Guest Editor: Zoe Courville, U.S. Army Engineer Research and Development Center Cold Regions Research and Engineering Laboratory, Hanover, NH, USA

Knowledge Domain: Atmospheric Science

Part of an Elementa Special Feature: The Multidisciplinary Drifting Observatory for the Study of Arctic Climate (MOSAiC)

Published: March 16, 2022 **Accepted:** February 7, 2022 **Submitted:** August 27, 2021

ELEMENTA Science of the Anthropocene

Elem Sci Anth is a peer-reviewed open access journal published by University of California Press.

OPEN ACCESS